Talanta 238 (2022) 123039

Contents lists available at ScienceDirect

Talanta

journal homepage: www.elsevier.com/locate/talanta

Magnetic nanoparticle modified electrodes for voltammetric determination of propellant stabiliser diphenylamine

Colm McKeever [a], Sarah Callan [a], Susan Warren [b], Eithne Dempsey [a,*]

[a] Department of Chemistry, Kathleen Lonsdale Institute for Human Health Research, Maynooth University, Maynooth, Co. Kildare, Ireland
[b] CREST Technology Gateway, FOCUS Research Institute, Technological University Dublin, Kevin St., Dublin, Ireland

ARTICLE INFO

Keywords:
Magnetite (Fe_3O_4)
Diphenylamine
Firearm residue

ABSTRACT

The overall aim of the work was to advance electrochemical devices capable of analysis of forensically relevant residues using rapid electrochemical sensor technology. In order to achieve this, electrochemical detection of the propellant stabiliser diphenylamine (DPA) was achieved via voltammetry with signal enhancement realised in the presence of iron oxide nanoparticle modified transducers. This allowed both mechanistic and analytical evaluation with the aim to achieve the required selectivity and sensitivity for reliable detection. DPA electrochemistry was examined at glassy carbon electrodes in aqueous (3:7 methanol: sodium acetate pH 4.3) electrolyte via potential sweeping, with an irreversible wave at $E_p = 0.67$ V *vs.* Ag/AgCl. The diffusion coefficient (D) for the oxidation process was calculated as 1.43×10^{-6} cm^2 s^{-1} with $\alpha n_a = 0.7$. DPA electrochemistry in a non aqueous methanol/acetonitrile electrolyte resulted in a D value of 5.47×10^{-8} cm^2 s^{-1} with $\alpha n_a = 0.5$. Electrochemical preparation of magnetic iron oxide nanoparticles was achieved via electrooxidation of an iron anode in the presence of an amine surfactant followed by characterisation with SEM/EDX, XRD, FTIR and thermal analysis. A surface confined layer of these magnetic nanoparticles served to positively influence the response to DPA while impeding formation of surface confined oxidation products, with generation of an improved analytical signal - sensitivity 1.13×10^{-3} A cm^{-2} mM^{-1} relative to bare electrode response (9.80×10^{-4} A cm^{-2} mM^{-1}) over the range 0.5–50 μM DPA using differential pulse voltammetry, with LOD 3.51×10^{-6} M and LOQ 1.17×10^{-5} M. Real sample analysis involved recovery and differential pulse voltammetry of unburnt and burnt gunshot residue with DPA qualitative and quantitative analysis.

1. Introduction

Global terrorism and rising gun crime demands decentralised microanalytical devices which enable sensitive and rapid detection of explosives and propellants relevant to firearm residue. Confirmation of traces of organic gunshot residue (OGSR) on individuals/clothing can establish whether a contact with explosives has occurred, with such results being often used as court evidence [1–3]. The residue consists of burnt and unburnt particles from the primer/propellant with the inorganic fraction typically consisting of Ba, Sb and Pb particles while the organic fraction includes burnt or unburnt particles consisting of propellants nitroglycerin, nitrocellulose in addition to stabilisers such as ethyl or methyl Centralite (1,3-diethyl-1,3-diphenylurea (EC)) and diphenylamine (DPA) [4]. The latter are added to the propellant to remove nitrogen oxides produced by degradation of nitrocellulose and nitro-glycerine and prevent auto catalytic decomposition of the propellant [5]. Organic compounds that are vaporised during the firing process and then re-condense are less prone to secondary transfers due to adhesion to the skin.

Electrochemical techniques can be exploited in portable analytical systems capable of miniaturisation with fast time to result and lend themselves well to dual detection of the metallic and OGSR components, extending analytical approaches available for onsite detection of volatile chemical markers with improved detection of explosives. Such forensic devices have been subject of a recent review by Pereira de Oliveira et al., 2018 and specifically the electrochemical detection of explosives by Yu et al., 2017 [6] and analysis of gunshot residue by Dalby et al., 2010 [7]. Speed of analysis following sample recovery is key to prevent compound degradation, resulting in chemical profiling and provision of evidence of firearm origin and source of ammunition.

DPA analysis has attracted interest in both forensic [8] and environmental [9] areas in recent years. It is most commonly used as a

* Corresponding author.
E-mail address: eithne.dempsey@mu.ie (E. Dempsey).

https://doi.org/10.1016/j.talanta.2021.123039
Received 9 July 2021; Received in revised form 2 November 2021; Accepted 3 November 2021
Available online 6 November 2021

stabilising agent for propellent systems in ammunition where it binds to the propellant degradation products, increasing the shelf life of the ammunition. DPA is also commonly used to aid in the storage of harvested apples preventing a storage disorder called "scald". DPA has become more prevalent in recent years as an emerging concern with regards to environmental pollution. The European Union first implemented a limit on the use of DPA in 2008 and Commission Regulation 2018/1515 [10] limits the presence of DPA on nearly all food items to 0.05 mg/kg, implemented from 1st of May 2019.

Due to ubiquitous background metal residues in the environment [5] the sole dependence on metal dissolution from a forensic swab with subsequent electrochemical processing is risky. This is in contrast with the extremely low residual/background levels of components of the organic fraction of gunshot residue and due to new regulations and limits residual DPA will become more closely monitored environmentally. Therefore, there is a growing interest to integrate metal electroanalysis with organic residue analysis (stabilisers/propellants) realising a more robust analytical approach [11]. Maitre et al. studied the persistence of organic residues on shooter's dominant and non-dominant hands over time and found that the observed trends for organic gunshot residue were similar to those observed with the inorganic residue, with three compounds of interest (DPA, *N*-nitrosodiphenylamine (*N*-nDPA) and EC) still being observed in >70% of samples up to 4 h after firing with the aid of UPLC-MS/MS analysis [12]. The *N*-nDPA derivative of DPA is formed as a result of nitration of DPA involving degradation products of nitro-glycerine. A better understanding of the degradation of smokeless powder and OGRS could allow identification of degradation products characteristic of OGSR [13].

The redox behaviour of DPA (predominately non-aqueous) has been studied in previous reports [12,14–16] with there being very few reports of its detection at modified electrode surfaces [17]. Renewed interest as a forensically significant target molecule is the incentive behind this work and it is thus an important starting point for the development of an analytical method for the complex array of compounds found in organic component of the residue. Here, we evaluate the redox electrochemistry of DPA at glassy carbon transducers and examine magnetic nanoparticles (MNP) as electrode modifiers, to aid DPA detection. Among these materials, magnetite (Fe_3O_4), a Fe^{2+} and Fe^{3+} complex oxide, is one of the most commonly studied super-paramagnetic nanoparticle, being widely used in magnetic resonance imaging contrast enhancement, tissue specific release of therapeutic agents [18], in addition to *in vitro* binding of proteins and enzymes [19].

Magnetic nanoparticles allow ease of separation in solution [20] while acting as effective electrode modifiers [21] with applications in medical imaging [22] drug delivery [23] biosensing [24,25] and bioanalytical devices [26]. The latter are the subject of a recent review by Hasanzadeh et al. *2015* [27]. MNP can have particle size ranging 10–50 nm [28] and present different physico/chemical properties compared to their bulk size, due to the size differences. The material has been successfully modified or doped with Cobalt [29] and Manganese [30], however sensor approaches based on the unmodified form have received little attention.

Methods to prepare iron oxide include chemical precipitation, gas phase condensation, thermal decomposition of organometallic compounds and electrochemical techniques. In this work we utilised an electrosynthetic approach (with the aid of an iron anode and cathode) as it is a facile, rapid and well controlled process realising good yields. This has been subject of a recent review by Raminoghadam et al. 2014 [31] and concentration and nature of electrolyte and current density affect the size and morphology of nanoparticles produced [26,32]. There are fewer reports on the electrosynthesis of MNP relative to solution-based approaches with the former having the advantages of speed, control and consistency. Here the method of Cabrera et al., 2008 [33] was adapted for the electrosynthesis of MNP which were subsequently characterised via surface, thermal and electrochemical means after which they were immobilised onto GCEs for diphenylamine measurement using cyclic voltammetry and differential pulse voltammetry. The work includes an investigation into the redox behaviour of DPA in aqueous and organic supporting electrolytes which shines a light onto by-products of the oxidation process at carbon, platinum and MNP modified electrodes. To the best of our knowledge, this is the first such report of the use of MNPs as electrocatalysts in aromatic amine oxidation, enabling signal amplification while limiting follow on homogeneous processes which resulted in deposited polymeric species. The chemical sensor proposed here also represents the first modified electrode designed and optimised for propellant stabiliser electroanalysis with real sample residue recovery and analysis. This work paves the way towards a sensitive multiplexed quantitation strategy for OGSR which relies on signal discrimination, appropriate limits of detection and robust sensing strategies suitable for laboratory or field deployment. Thus, the data presented provides an important stepping stone in our quest to realise a rapid and portable analytical test for forensic chemical analysis of OGSR.

2. Experimental

2.1. Instrumentation and reagents

The surface morphology of the magnetic nanoparticles was measured using SEM (Hitachi SU-70 FE-SEM with Oxford instruments X-max 50 mm^2 Solid state detector. XRD was performed by Wynette Redington at University of Limerick using a PANalytical Empyrean-reflection instrument. ATR was performed on a Thermo Scientific iS50 ATR. Thermal analysis was performed using a PerkinElmer STA 6000 DSC/TGA analyser. All electrochemical experiments were carried out using the Solartron Potentiostat Model 1285 operated by Scribner Associates CorrWare software package with data analysis using CorrView Version 2.3a. An IR lamp was used to dry the magnetic nanoparticle suspensions on GCEs and a ThermoFisher thermostatic oven was used for drying the magnetic nanoparticles following preparation. UV–Vis studies were performed using a PerkinElmer Lambda 35 UV/VIS Spectrophotometer, and a spectroelectrochemical (SEC) cell [Path length (0.1 cm)] with platinum gauze working electrode (geometric area 0.96 cm^2).

Ethanol (anhydrous ≥99.5%), Methanol (ACS Reagent, 99.8%), diphenylamine (ACS Reagent ≥99%), acetic acid (ACS Reagent ≥95.0%), lithium perchlorate (ACS Reagent ≥95.0%) were all purchased from Sigma Aldrich and required no further purification. Electrode polishing solution was a 1 μM Monocrystallin diamond suspension (Akasel). The sacrificial iron anode and cathode rods (3 × 12 cm^2) were purchased from Goodfellow (purity 99.5%). A glassy carbon electrode (GCE) (3 mm disk 0.0707 cm^2) served as the working electrode, while platinum wire and a standard Ag/AgCl electrode (internal solution 3 M KCl) were employed as the counter and reference electrodes, respectively. The Ag/AgCl reference electrode was stored in 3 M KCl when not in use. A non-aqueous reference electrode was prepared using silver nitrate (10 mM) and lithium perchlorate (0.1 M) in methanol/acetonitrile.

2.2. Procedures

2.2.1. Electrochemical procedures

The aqueous electrolyte employed was 0.1 M $LiClO_4$ in methanol and sodium acetate buffer solution pH 4.5 (30:70) (37 mL sodium acetate (0.1 M) and 63 mL acetic acid (0.1 M) realised a solution of pH ~ 4.5) while the non-aqueous electrolyte was 0.1 M $LiClO_4$ in methanol and acetonitrile (50:50). Cyclic voltammetry was performed over the relevant potential range with GCE selected as working electrode. The working electrodes were prepared by polishing with diamond paste slurry (1.0 μm), followed by washing in deionised water and air dried.

2.2.2. Synthesis of magnetite particles

The facile electrochemical preparation of magnetic iron oxide nanoparticles was achieved via electrooxidation of an iron anode in the

presence of an amine surfactant pH 5.7 (adapted from method by Cabrera et al., 2008 [33] and Rahimdad et al. 2019 [34]. The sacrificial iron anode and cathode rods (99.5% purity) was first polished mechanically using sandpaper in order to remove impurities, then transferred into a water/ethanol mixture (50:50 v/v) followed by ultrasonication for 20 min to ensure no further impurities were present. A potential of 5 V was applied for 1800 s in 0.04 M tetramethylammonium chloride as electrolyte/capping agent with temperature control using a water bath held at 60^{O}C. The interelectrode spacing was 8 mm (edge to edge) using a 9.4 mm diameter iron anode and cathode with immersion depth 3 cm (see Scheme 1). During the electrosynthetic process the solution changed from yellow to brown with eventually a black precipitate forming according to the processes below:

$$Fe\ (s) \rightarrow Fe^{2+}\ (aq) \rightarrow Fe^{3+}\ (aq) + 3e^{-}\ (anode)$$

$$H_2O\ (l) + 2e^{-} \rightarrow H_2\ (g) + 2OH^{-}\ (aq)\ (cathode)$$

$$Fe^{3+}\ (aq) + 3OH^{-}\ (aq) \rightarrow Fe(OH)_3\ (s)$$

$$3Fe(OH)_3\ (s) + H^{+}\ (aq) + e^{-} \rightarrow Fe_3O_4\ (s) + 5H_2O\ (l)$$

The MNPs (~129 mg yield under optimum conditions) were allowed to settle in the solution (aided by magnets) decanted and washed with water ×3, followed by ethanol ×3. This process was repeated until the supernatant was clear with a final ethanol wash. The particles were collected and allowed to dry in an oven at 80^{O}C for 3 h followed by suspension in ethanol at 1 mg mL^{-1}.

2.2.3. Electrode modification

A polished GCE (using a 1 μM monocrystalline diamond suspension) was rinsed with ethanol and allowed to dry under an IR heat lamp. The magnetite suspension (1 mg mL^{-1} in ethanol) was sonicated to ensure an even dispersion of particles and drop casted onto the electrode surface in 5 × 20 μL increments with drying in between and loading at 1.416 mg cm^{-2}. Lower loadings (2 × 20 μL) resulted in poor signal and surface stability.

2.2.4. Spectroelectrochemistry UV–Vis studies

A Pt gauze electrode was electrochemically cleaned in 0.5 M H_2SO_4 by cycling for 20 cycles at 200 mV s^{-1} followed by mechanical polishing using 1 μM monocrystalline diamond suspension. Voltammetric studies utilised the spectroelectrochemical cell over the potential range −1 to 1 V at 100 mV s^{-1} for 100 cycles in the aqueous electrolyte with 1 mM DPA. Both the modified electrode and the solution remaining following deposition were analysed by UV–Vis spectroscopy over the range 200–700 nm.

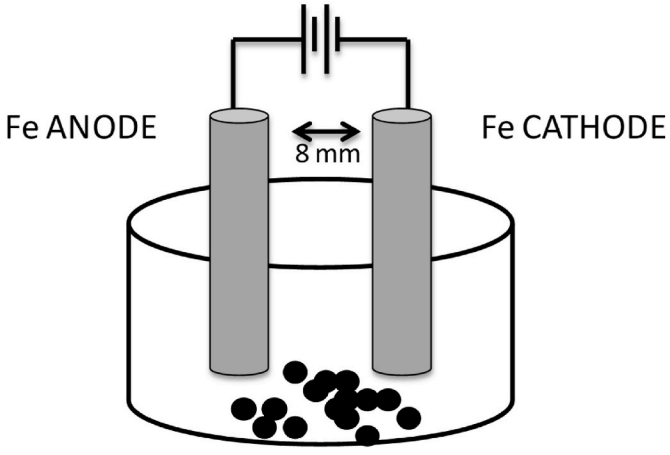

Scheme 1. Fe anode and cathode rods immersed in tetramethylammonium chloride with electrochemical formation of Fe_3O_4 upon application of 5 V for 30 min at 60 °C.

2.2.5. Surface analysis

Particle size and morphology was analysed using a Hitachi SU-70 FE-SEM from a 1 mg mL^{-1} MNP sample in ethanol. Average particle size was determined based on measurement of 100 particles.

2.2.6. Differential pulse voltammetry for standard and sample analysis

Differential pulse voltammetry was performed at bare and modified GCEs in supporting electrolyte with initial potential −1 V final potential 1.5 V, incremental potential 0.004 V, Amplitude 0.05 V, pulse width 0.05 s, sample width 0.0167 s, pulse period 0.5 s.

2.2.7. Firearm residue extraction and analysis

A portion of fabric was subjected to close range firing using a shotgun - cartridge Maxam© CSB 3 powder, a single base powder that is fast-burning specially indicated for loading low shot weight shotshells (up to 32 g). The unfired propellant specifications are given below (Table 1) [35].

Gunshot residue recovery involved application of a methanol-soaked cotton swab over a designated area (50 cm^2) of the textile sample. The swab was added to a volume of methanol and sonicated for 30 min. The extracted solution was filtered (gravity filtration) to remove remaining particulates and the solvent removed under Nitrogen. The remaining white solid was reconstituted in 1.5 mL methanol and brought up to 5 mL with 0.1 M $LiClO_4$ sodium acetate buffer pH 4.4 (retaining the 3:7 electrolyte employed with the standards). A spent cartridge was subjected to dry cotton swabbing followed by extraction as above. Preparation of an unburnt propellant sample involved taking 5.9 mg (six discs) of the unfired propellant powder and sonicating in methanol, filtration and making up in supporting electrolyte as per procedure above. DPV followed in all cases and samples were subjected to spiking for quantitative analysis via standard addition.

3. Results and discussion

3.1. Optimisation of electrochemical synthesis conditions for magnetic nanoparticle formation

The influence of applied potential (1, 2.5 and 5 V) at 60 °C (for 30 min) and temperature (45 °C, 60 °C and 75 °C) at 2.5 V (for 30 min) was examined during the electrochemical preparation process. Fig. 1 shows the current-time response evident during MNP electrochemical formation under three applied potential conditions, with gradual stabilisation of the current passed over the 30 min electrosynthesis period. Product yield was 98 mg (1 V), 254 mg (2.5 V) and 141 mg (5 V). Material formed under high temperature resulted in higher Fe oxidation state impurities which necessitated lengthy cleaning steps. Overall, the condition which resulted in minimal impurities and highest quality of

Table 1
Unfired propellant specifications as per manufacturer.

Gauge	Powder (g)	Lead	Velocity (m/s)	Pressure (bar)
12	1.65	30	409	552
Shape	**Colour**	**Dimension**	**Thickness**	**Density**
Disc	Grey	1.7 mm	0.3 mm	535 g/L

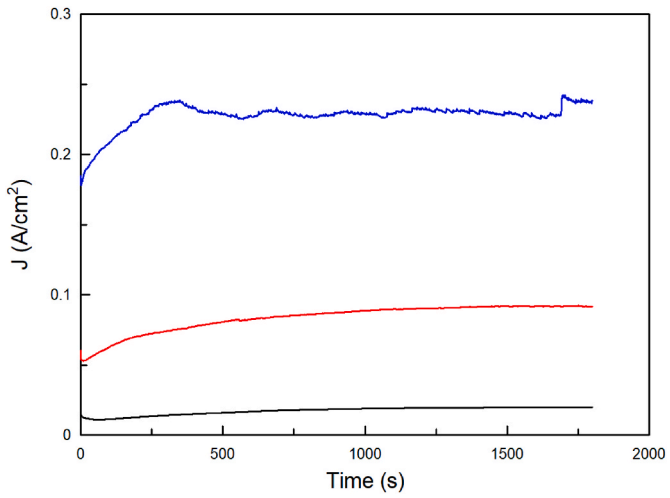

Fig. 1. Current-time response during the electrosynthetic process for MNP production at iron anode and cathode. A potential of 1, 2.5 and 5 V ((black, red and blue trace), was applied for 1800 s in 0.04 M tetramethylammonium chloride at 60 °C. The interelectrode spacing was 8 mm (edge to edge) using a 9.4 mm diameter iron anode and cathode with immersion depth 3 cm. (For interpretation of the references to colour in this figure legend, the reader is referred to the Web version of this article.)

material (verified by FTIR and SEM) was achieved using 5 V at 60 °C and hence this conditions was employed for the remainder of the study.

3.2. Spectroscopic and surface characterisation of magnetic nanoparticles

FTIR spectroscopy was used in order to obtain information about the nature of surface hydroxyl groups and adsorbed water (SI(1) A and B). Hydroxylation of iron oxides is followed by further adsorption of water molecules which interact via H bonding to the surface OH groups. Tertiary amine C–N stretch 1125 cm^{-1} (1250-1020 cm^{-1}), intermolecular bonded O–H stretching 3409 cm^{-1} (3550-3200 cm^{-1}) and OH bending vibration 1636.8 cm^{-1} (1652.88 cm^{-1}) were evident. The characteristic vibrational bands of pure Fe_3O_4 mainly appeared at 561 and 421 cm^{-1} (literature values of 572 and 377 cm^{-1} [36] being attributed to Fe–O vibrations and those at 422 and 611 cm^{-1} ascribed to Fe–O bending vibrations of Fe_3O_4 [36].

Thermogravimetric analysis (TG) and differential scanning calorimetry (DSC) (Fig. 2.) (30–640 °C) was used to examine the thermal stability of the material which can depend on grain size and the

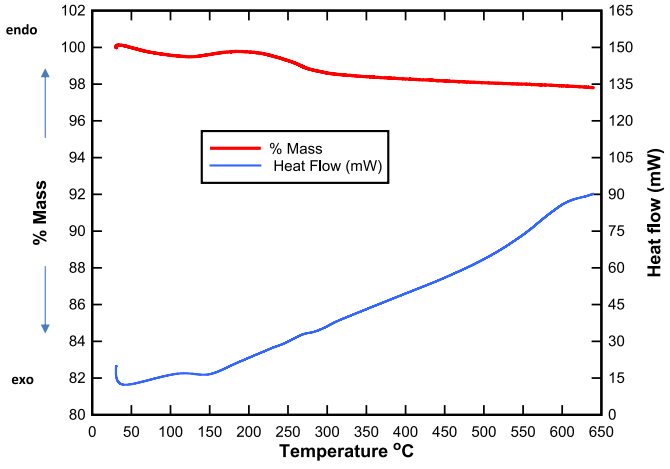

Fig. 2. Thermogravimetric and differential scanning calorimetry of a 12.35 mg Fe_3O_4 sample from ambient to 650 °C at 10 °C min^{-1} in air.

synthetic process [32]. The initial mass variation loss (red TG curve Fig. 2.) may be due to an overlap of the exothermic process of H_2O and surface –OH group elimination with an exothermic DSC change at 100 °C followed by the oxidation of Fe(II) to Fe(III) as magnetite $[Fe^{2+}Fe_2^{3+}]O_4$ changes to maghemite $\gamma Fe_2^{3+}O_3$. The second DSC exothermic (oxidation) signal was a weak process at 290.39 °C ($\Delta H = -4.157$ J g^{-1}) and finally an endothermic event at 606.74 °C ($\Delta H = -4.157$ J g^{-1}) occurred close to the upper temperature limit of the sample crucible employed. Across the range 170–650 °C the overall mass loss was 2.05%, below that of the theoretical 3.1% expected for conversion of magnetite to maghemite.

SEM and EDS analysis together provided information regarding morphology and elemental composition of the MNP with micrometric scaled aggregates of the nanoparticles evident. SEM images (Fig. 3(A-D)) confirm the nanoparticle size and spherical nature of particles prepared using application of 1, 2.5 and 5 V for 30 min at 60 °C with median distribution plot (E) and average values 55.1, 49.6 and 50.7 nm respectively (Table 2). The nanomaterial prepared from 5 V resulted in relatively tighter size distribution.

Elemental identification was in agreement with the synthetic composition. EDS (SI(2)) spectra for each material were normalised by oxygen stoichiometry resulting in 75.4 Fe: 23.3 O (1 V MNP), 75.5 Fe:23 O (2.5 V MNP) and 77.1 Fe: 22.5 O (5 V), which align with the theoretical atomic mass ratio for Fe_3O_4 (72.4 Fe:27.5 O).

XRD analysis (SI (3)) was performed with broadening visible indicating small crystallites with characteristic peaks matching well with literature values [37,38] for 220, 311, 400, 511 and 440 (see SI (3) Table.) crystal planes of Fe_3O_4 spinal face centred cubic crystal structure [39] with both Fe^{2+} and Fe^{3+} occupying octahedral sites and Fe^{3+} tetrahedral sites. Phase identification of magnetite and maghemite (γ-Fe_2O_3) is challenging as both have the same cubic structure with close lattice parameters [40].

3.3. Electrochemical characterisation of magnetic nanoparticles

Fig. 4 shows voltammograms of the bare and modified GCEs (as described in section 2.2.3)) examined in 0.1 M KCl, over the potential range −1 to +1 V vs. Ag/AgCl at 50 mV s^{-1}. Fig. 4(A) shows CVs for electrodes modified with MNP synthesised at different applied voltages while Fig. 4(B) examines the redox properties of the materials prepared under different temperatures. Hydrogen adsorption/desorption was evident in all cases between −0.5 and −1.0 V which corresponds to literature (Yuan et al. [41]). An irreversible anodic wave was observed at 1.0 V vs Ag/AgCl. During a cathodic scan, it has been shown Fe_3O_4 can undergo dissolution with release of Fe^{2+} which can be electrochemically re-oxidised (1.0 V vs Ag/AgCl in this electrolyte) with this process shown to be more evident at lower pH, and dependent on both the presence of oxygen in solution and the cathodic potential limit. Further studies focused on use of methanol/sodium acetate buffer (3:7) as electrolyte to provide compatibility with the optimum DPA dissolution solvent and more clearly defined Fe^{2+} reoxidation signals.

A voltammogram of bare and modified electrodes was performed in aerated and degassed aqueous electrolyte (in methanol/sodium acetate buffer (3:7)) (Fig. 5(A)). The black curve representing the MNP modified GCE in aerated electrolyte resulted in a strong irreversible redox process at $E_{p(a)} = 0.5$ V with weak reduction wave at 0.0 V vs. Ag/AgCl. This is thought to represent re-oxidation of Fe^{2+} released from $[Fe^{2+}Fe_2^{3+}]O_4$ following the cathodic sweep and the signal was supressed in degassed electrolyte (Fig. 5(A)). It has been shown previously [37] that this anodic peak increased upon addition of Fe^{2+} to the cell and was found to be pH dependent.

Fig. 5(B) shows the influence of the cathodic limit on this anodic process with no couple evident when swept to 0.0 V (lower limit) and a weak process following −0.5 V (lower limit) vs. Ag/AgCl, indicating that a −1.0 cathodic limit was required to register this anodic process.

Fig. 6 shows a scan rate study (20-200 mVs^{-1}) of the MNP modified

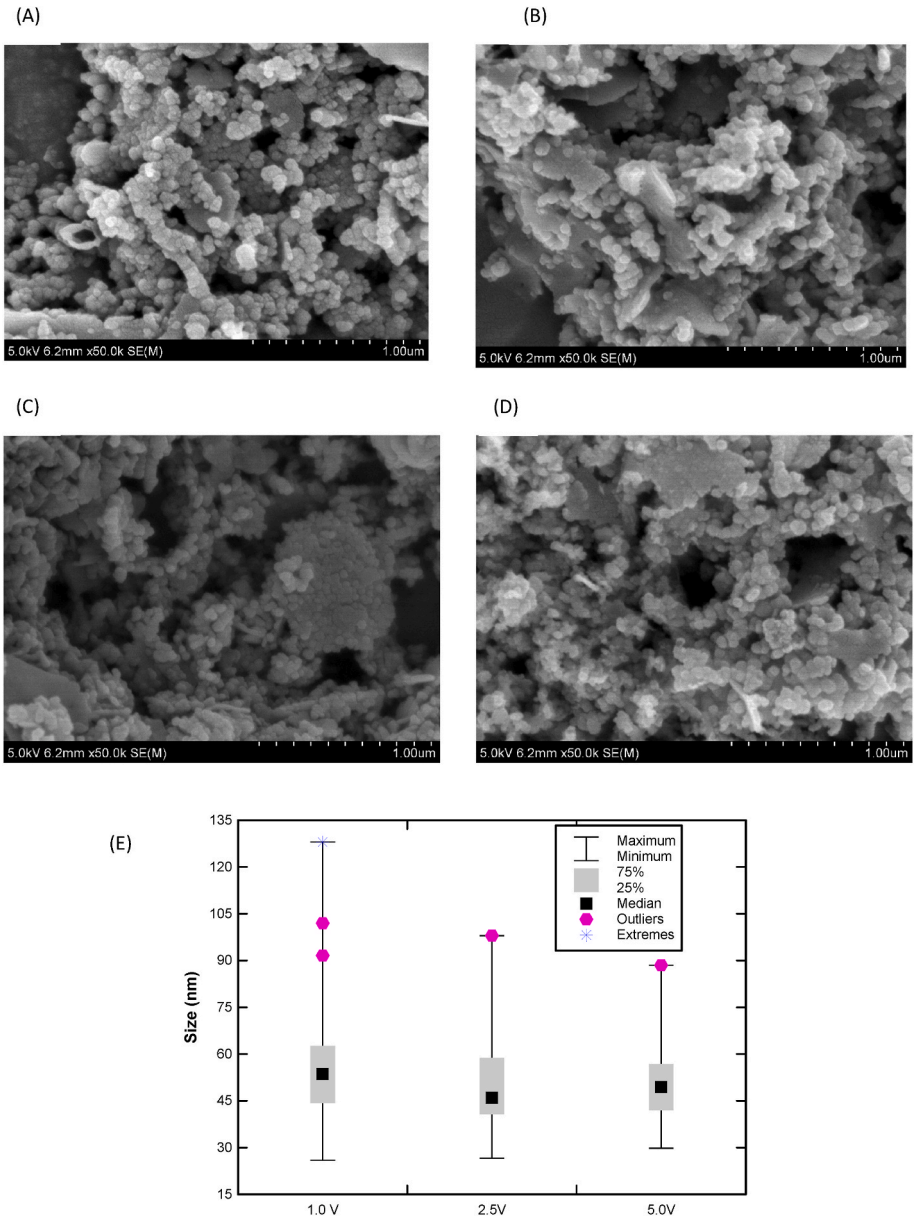

Fig. 3. High resolution SEM images of Fe_3O_4 nanoparticles with electrosynthesis via application of 1 V (A) 2.5 V (B) and 5 V (C, D). Particle size distribution based on 100 particles (1 V), 50 particles (2.5 and 5 V) samples.

Table 2
Average size of MNP prepared via electrosynthesis.

	1 V	2.5 V	5 V
Average (nm)	55.1	49.6	50.7
Stdev	16.0	13.7	12.4
Max (nm)	128.0	98.0	88.5
Min (nm)	25.9	26.6	29.8

GCE resulting in a linear relationship ($r^2 = 0.993$) between current taken at 0.6 V and scan rate (Vs^{-1}) with slope of 1.01×10^{-3} A cm^{-2} $V^{-1}s$ resulting in a surface coverage value of 1.08×10^{-9} mol cm^{-2} using the relationship below (1) for a one electron surface confined species. A plot of current vs. square root scan rate showed linearity (up to 0.3 Vs^{-1}) indicating a mixed diffusional system, correlating with the concept that Fe^{2+} release diffuses to the electrode for re-oxidation at 0.5 V vs. Ag/AgCl. Log current *vs* log scan rate plots resulted in a slope of 0.82 over the range 0.05–0.5 V s^{-1} which is more typical of an adsorbed species (slope 1.0). The magnetite layer exhibited capacitance of 2×10^{-4} F cm^{-2} which was 3.3 times that of the electric double layer capacitance – being in line with recent literature [42].

$$I_p = \frac{n^2 F^2}{4RT} A\nu\Gamma \quad (1)$$

A stability study was performed by cycling the modified electrode over the range −1 to +1 V vs. Ag/AgCl for 40 cycles in 3:7 methanol: sodium acetate buffer at 100 mVs^{-1}. A continuous decrease in current was evident (data not shown) which possibly reflects a transformation process upon cycling resulting in lower Fe^{2+} release following the first reduction step. The experiment was repeated following addition of 20 μL of 1% Nafion to the MNP layer in an attempt to improve stability; however similar reduction in the main redox process was evident with a 96% loss of the initial current after 20 cycles at 100 mV s^{-1}. The lower potential limit was required in order to visualise impact on the anodic process (Fe^{2+}/Fe^{3+}) to the detriment of the signal. The electrocatalytic effect of the surface confined material was thought to be intact despite

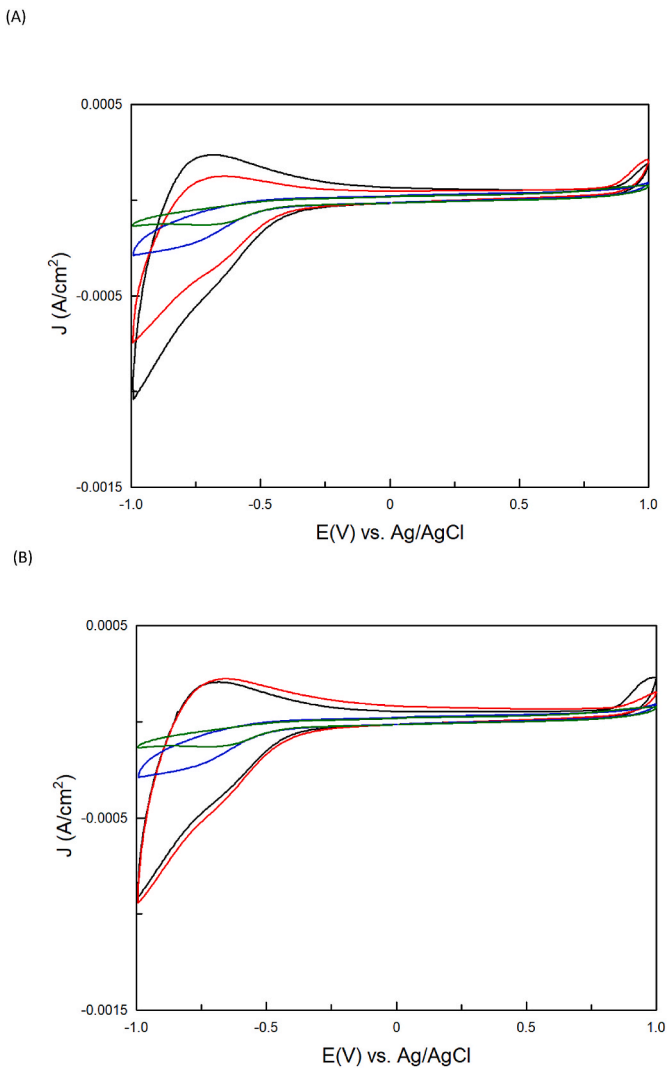

Fig. 4. (A) Cyclic voltammogram of MNP modified GCE and bare electrode over the potential range −1 to +1 V vs Ag/AgCl at 50 mV s^{-1} in 0.1 M KCl. Green trace – bare electrode, blue trace – modified electrode with MNP synthesised at 5 V, red trace - modified electrode with MNP synthesised at 2.5 V, black trace - modified electrode with MNP synthesised at 1 V. (B) Cyclic voltammogram of MNP modified GCE (MNP prepared at 5 V) and bare electrode over the range −1 to +1 V vs Ag/AgCl at 50 mV s^{-1}. Green curve – bare electrode, blue curve, red curve and black curve – modified electrode with MNP synthesised at 60 °C, 75 °C, 45 °C respectively. (For interpretation of the references to colour in this figure legend, the reader is referred to the Web version of this article.)

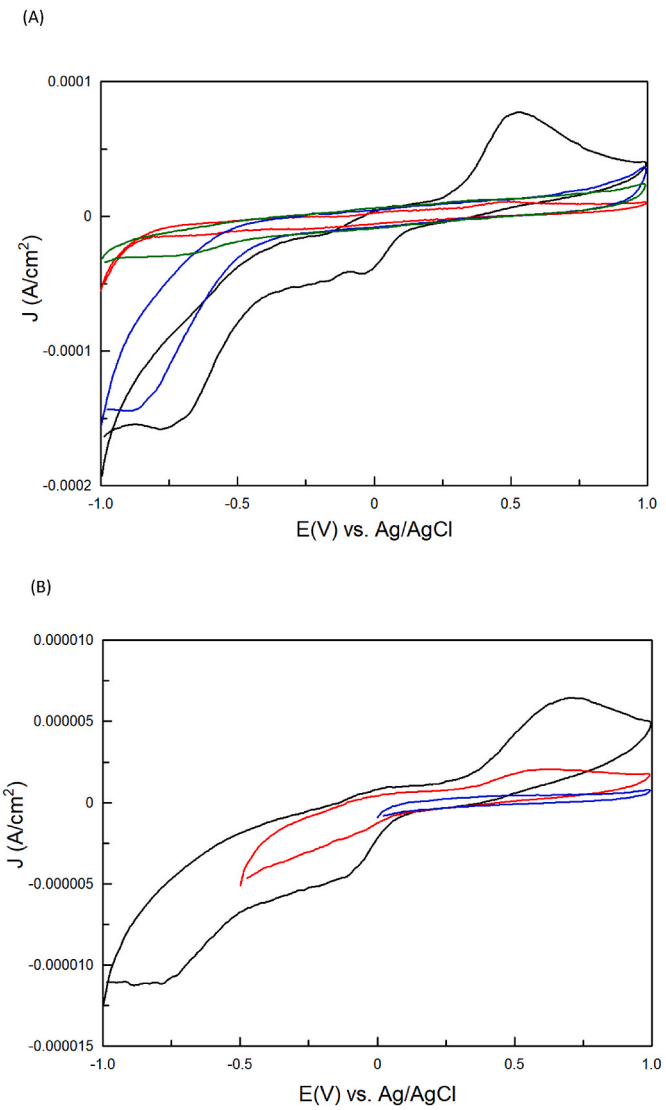

Fig. 5. (A) Cyclic voltammogram of bare and MNP modified GCE over the range −1 to +1 V vs. Ag/AgCl at 50 mV s^{-1} in methanol/sodium acetate buffer (3:7). Black trace – modified electrode, red trace - modified electrode (degassed), blue trace – bare electrode, green trace – bare electrode (degassed). **(B)** Influence of cathodic potential limit on MNP redox behaviour from 0 to 1 V (blue), −0.5–1 V (red) and −1 to 1 V (black) vs. Ag/AgCl at modified GCE. (For interpretation of the references to colour in this figure legend, the reader is referred to the Web version of this article.)

these surface alterations.

3.4. Electrochemical examination of diphenylamine

Non aqueous electrochemistry of diphenylamine was examined in methanol:acetonitrile (1:1) in 0.1 M $LiClO_4$ over the concentration range 0.05–1 mM at 50 mVs^{-1} (Fig. 7(A)). The anodic peak at 0.6 V corresponded to the one electron oxidation of the aromatic amine resulting in diphenylamine radical cation formation (stabilised in resonance forms) with recombination resulting in formation of a diphenylbenzidine dimer (DPB). Dimerization occurs via C–C addition in the para position (Scheme 2) and the DPB species itself is electroactive displaying a weak oxidation (E_p = 0.45 V) and reduction process (E_p = 0.3 V) being most evident at higher concentrations [11,40]. A plot of Ip(a) vs concentration was linear (0.05–1 mM) based on the main anodic process at 0.65 V with sensitivity 0.374 A cm^{-2} M^{-1} (r^2 = 0.9955).

A scan rate study was performed over the range 50–500 mVs^{-1} (−1 to +1 V vs. Ag/Ag^+) and Fig. 7(B) shows the response with a clear increase in current and associated shift in Ep(a) from 0.6 to 0.73 V vs. Ag/Ag^+. The ratio of anodic and cathodic currents for this process plotted *vs* scan rate indicates a ECE process – irreversible electron transfer followed by a homogeneous chemical reaction where the ratio decreased as the oxidised species was consumed by the subsequent chemical reaction (formation of diphenylbenzidine). Scan rate studies verified a diffusion controlled chemically irreversible process which may be described by Equation (2) [43]. The expressions below allowed estimation of diffusion constant (D) and transfer coefficient (α) (assuming n = 1) as 5.47 × 10^{-8} cm^2 s^{-1} with $\alpha n_a = 0.49$.

$$i_p = 2.99 \times 10^5 \times n \times \sqrt{\alpha n_a} \times A \times C \times \sqrt{D} \times \sqrt{v} \quad (2)$$

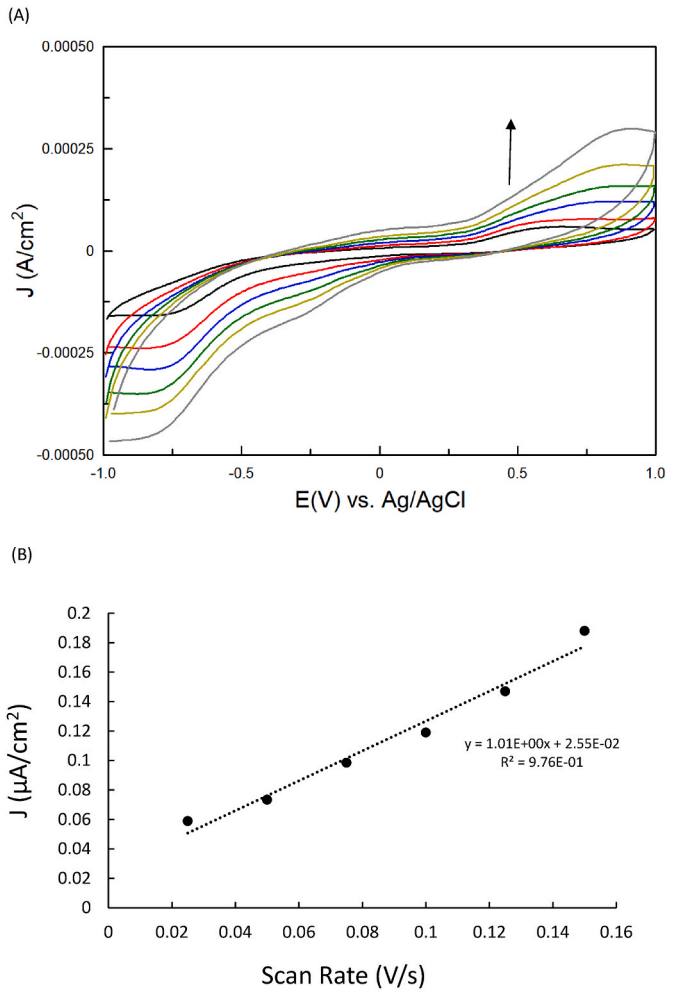

Fig. 6. (A) Scan rate study for MNP modified GCE (88 µg/cm^2 loading) over the range 20–200 mV s^{-1} in aqueous electrolyte (3:7 methanol: acetate buffer pH 4.5) (B) Corresponding scan rate plot.

$$E_p - E_{p\left(\frac{1}{2}\right)} = \frac{1.857 \times R \times T}{\alpha n_a \times F} \quad (3)$$

where α is the transfer co-efficient, n_a is the number of electrons in the rate determining step, D_o is the diffusion co-efficient and ν is scan rate.

Equation (4) allows determination of k^o (standard heterogeneous rate constant) for an irreversible process [43].

$$k^o = 2.415 \exp\left(-0.02\frac{F}{RT}\right)\sqrt{D_o}\frac{1}{\sqrt{(E_p - E_{p/2})}}\sqrt{v} \quad (4)$$

where k^o is the standard heterogeneous rate constant, R is the gas constant, T is temperature and F is Faraday's constant. Taking E_p at 50 mVs^{-1} as 0.61 V and $E_{p/2}$ at 0.561 V this results in a k^o value of 1.23 × 10^{-3} cm s^{-1}.

Following dissolution testing the most suitable aqueous solvent system was found to be 3:7 methanol: sodium acetate buffer (pH 4.5) representing a more suitable electrolyte for practical DPA sensing applications. A scan rate study in 1 mM DPA (Fig. 8(A)) showed oxidation at 0.7 V vs Ag/AgCl with more dominant electrochemistry evident for the surface confined follow-on product of the initial oxidation step at Ep (a) 0.47 and Ep(c) 0.35 V vs Ag/AgCl. The diffusion coefficient was calculated as 1.4 × 10^{-6} cm s^{-1} with an$_a$ = 0.7 and k^o = 4.08 × 10^{-4} cm s^{-1} which was 3 times lower than the rate constant in the organic electrolyte (literature D value 2.5 × 10^{-5} cm^2 s^{-1} [12]). A plot of log Ip

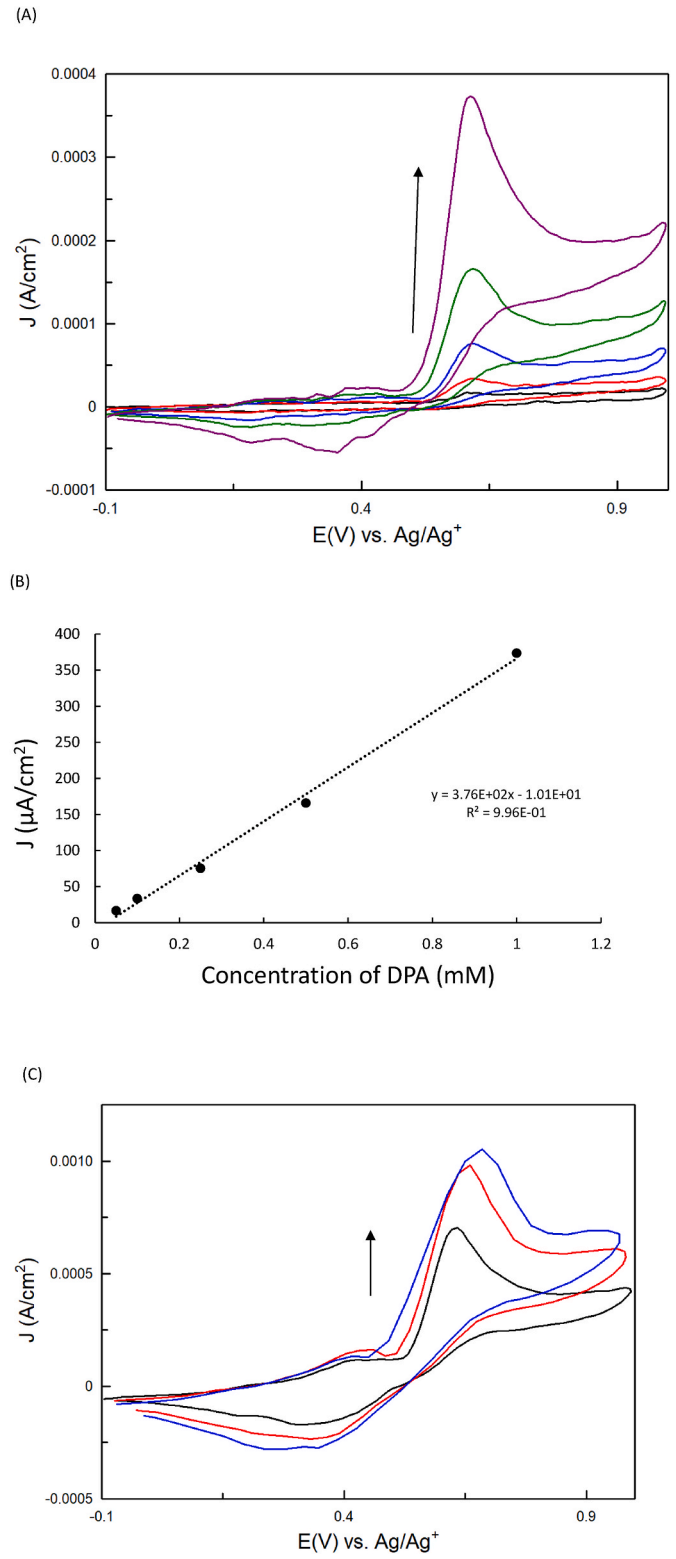

Fig. 7. **(A)** Voltammogram of DPA at an unmodified GCE over the concentration range 0.05–1 mM at 50 mV s^{-1} from −0.1 to 1 V at 50 mV/s in a 1:1 solution of acetonitrile:methanol with 0.1 M $LiClO_4$ with corresponding calibration plot **(B); (C)** Effect of scan rate on voltammetric response in 2.5 mM DPA over the range 0.1–0.4 V s^{-1} with an electrode cleaning step between scans.

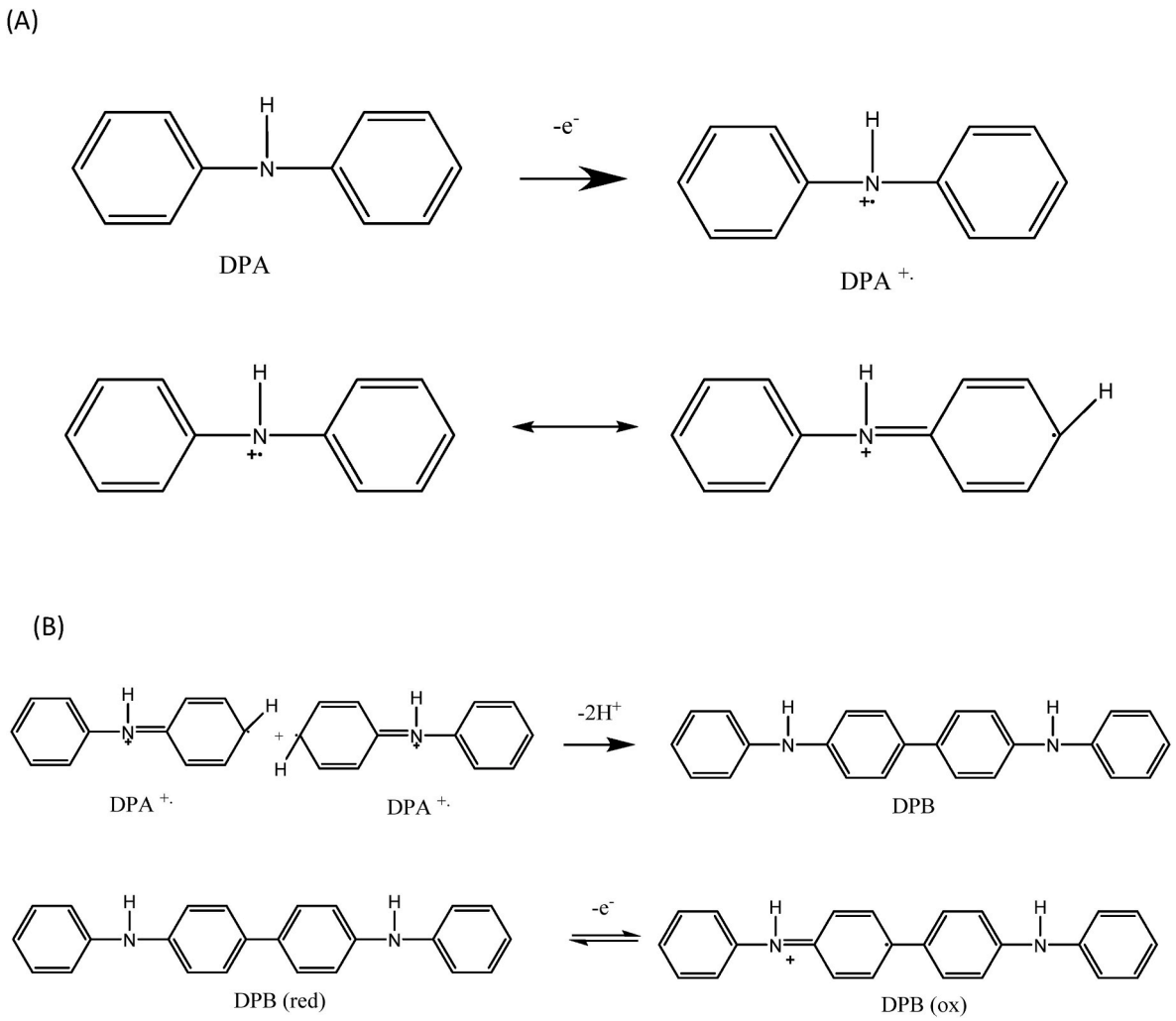

Scheme 2. (A) One electron oxidation of DPA to a radical cation (electrochemical step *E*) following which dimerization (chemical step *C*) and (B) leads to the electroactive diphenylbenzidine species (electrochemical step *E*) in non-aqueous electrolyte.

(c) for the surface confined cathodic process at 0.42 V vs. Log scan rate resulted in a slope of 0.7 while a plot of Ip(c) (E = 0.4 V) *vs* scan rate was found to be linear with $r^2 = 0.9966$ (SI(4)). The DPA concentration dependence of the anodic process resulted in a linear relationship over the range 0.1–0.6 mM (Fig. 8(B)) while the voltammogram of the deposited layer is shown together with dark field reflectance microscopy image (insert) in Fig. 8(C).

The visible appearance of films formed on the GCE surface in the methanol/sodium acetate buffer (3:7) leads us to believe that polymeric by-products of the DPA oxidation may form and contribute to this signal [17] resulting in electrochemical processes in line with previous diphenylamine electropolymerisation studies [44,45]. Formation of phenolic or benzoquinone products, the latter of which are common degradation species found in polyaniline films [46] may also occur in the acidic aqueous conditions examined and such derivatives may be responsible for the process evident at 0.47 V.

In order to examine this further, UV–Vis studies involved potential cycling in a 1 mM solution of the DPA monomer at a Pt gauze spectroelectrochemical working electrode. Absorption spectra (average n = 4) are shown (Fig. 9) and include (i) spectra taken of the solution following polymerisation and (ii) spectra recorded at the Pt gauze electrode in a spectroelectrochemical cell. Fig. 9(A) shows the absorbance spectrum before and after cycling in 1 mM DPA with reduction in the DPA signals (indicative λ_{max} for DPA are 204 and 284 [47]), and appearance of a shoulder at 332 nm and a weak absorbance at 455 nm (region II is shown in insert for clarity). Fig. 9(B) presents the data in absorbance ratio format with relative changes post cycling being evident at regions I and II of the spectra (Abs ratio >1) corresponding to 339 and 452 nm. Fig. 9(C) shows the spectrum over the range subject to most change at the Pt gauze electrode pre and post cycling with λ_{max} at 456 nm. In the case of the latter, background correction was ensured by using 1 mM DPA in the reference cuvette.

Deposition from 1 mM DPA onto Pt results in an unstable film which, while evident on the electrode at 456 nm (black curve Fig. 9(B) and (C)), results in a stronger signal for the solution spectrum (in the absence of electrode (red curve Fig. 9 (C)), with increase in the overall absorbance of the formed products (>312 nm). The UV studies point towards solution phase poly(diphenylamine) formation with λ_{max} that aligns well with literature values (subject to pH effects) [48–51] resulting from coupling of diphenylbenzidine species and appearing less adherent on platinum relative to carbon. Additionally, an understanding of the diphenylbenzidine formation is advantageous with respect to optical detection methods via the reaction of diphenylamine with nitrite and nitrate ions from nitrocellulose [52] with oxidation to the blue diamine.

Having established insights into the DPA oxidation process upon cycling, an evaluation of the influence of the electrosynthesised MNP on the DPA electrochemistry and quantitative signals follows, with the view to establishing optimum analytical performance parameters for the transducer prior to real sample analysis.

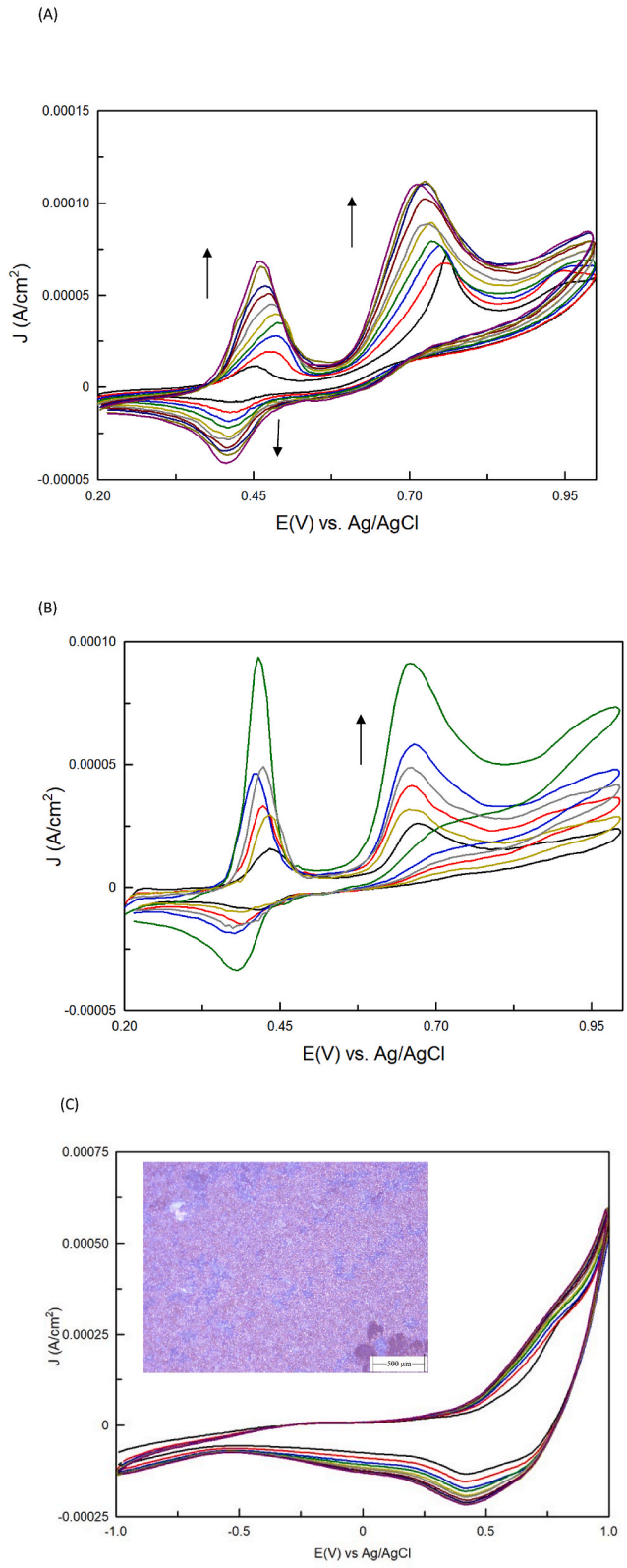

Fig. 8. (A) Scan rate study for 1 mM DPA in aqueous electrolyte over the range 5–50 mVs^{-1} with electrode cleaning between scans. **(B)** CV response to 0.1 mM additions of DPA with linear response for the irreversible anodic peak at 0.7 V. (C) film formed following cycling (electrochemistry shown in supporting electrolyte) with reflectance microscopy image on GCE (dark field)- cycles 1–10 shown 100 mV s^{-1}.

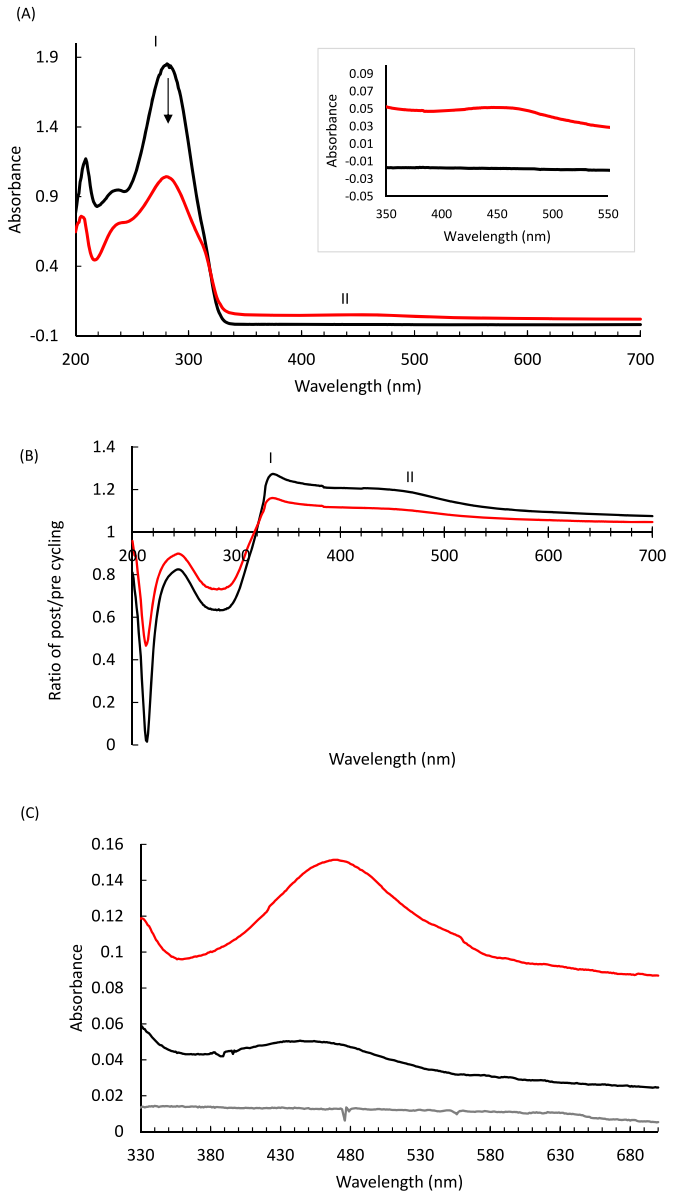

Fig. 9. (A): Spectra of DPA solution before (black) and after (red) cycling 100 times over the range −1 to 1 V at 100 mV/s. Indicative λ_{max} for DPA are 204 and 284 nm which decrease following film formation. (B) Absorbance ratio spectra for pre and post cycling solution with (red) and without (black) platinum gauze. (C) Overlaid spectra for Pt gauze background in background electrolyte (grey) and following cycling (black) with red curve representing solution only spectrum (background reference cuvette containing 1 mM DPA). (For interpretation of the references to colour in this figure legend, the reader is referred to the Web version of this article.)

3.5. Voltammetric response of diphenylamine at MNP modified electrode

The MNP was drop cast onto the GCE as described in section 2.2.3 and a voltammogram performed in 3:7 methanol:acetate buffer pH 4.5 in both aerated and degassed solutions over the range 0–1 V with no redox peaks evident over this range as described previously. Fig. 10(A) shows the response to 1 mM DPA in aqueous electrolyte at 50 mV s^{-1} over the potential range and −1 to +1 V (C) (with CVs for ranges 0.25 V (A) 0–1 V (B) shown in SI(5)). The MNP modified electrode resulted in an enhanced signal relative to the bare response (black curve vs red curve) with lowering of the anodic process evident at 0.5 V (34–63%) which appeared from cycle 2 onwards. Under optimum conditions over the range −1 to 1 V at 50 mV s^{-1} there was a 87–97% % (n = 3) increase

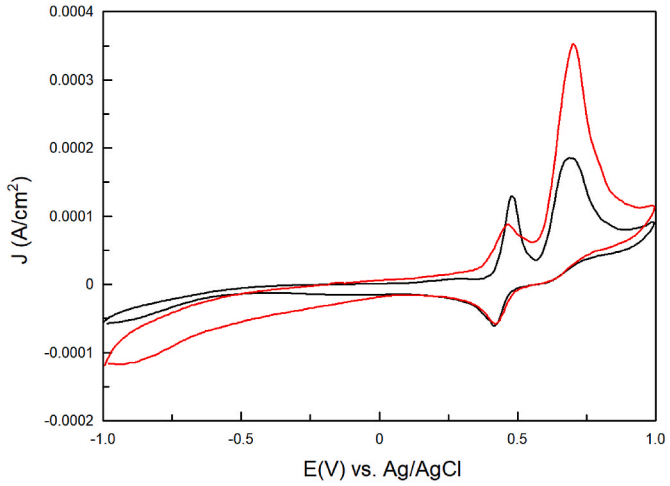

Fig. 10. Cyclic voltammogram of bare and MNP modified GCE over the range −1 to +1 V vs. Ag/AgCl at 50 mV s^{-1} in methanol/sodium acetate buffer (3:7). Black trace – Bare GCE, Red trace – MNP modified GCE. All voltammograms were recorded in the presence of dissolved O_2. (For interpretation of the references to colour in this figure legend, the reader is referred to the Web version of this article.)

in the DPA oxidation at Ep = 0.7 V relative to unmodified GCEs.

The apparent ability of the MNP layer to impede the diphenylbenzidine dependent polymer redox process (possibly due to stabilisation of $DPA^{+\cdot}$) was evident and can aid in sensor selectivity and reusability/surface regeneration as required. Linear sweep voltammograms resulted in calibration plots over the range 0.01–1 mM DPA (SI(6) with sensitivity of 5.10×10^{-4} A cm^{-2} mM^{-1} which is 1.51 fold increase relative to the bare electrode response (3.36×10^{-4} A cm^{-2} mM^{-1}) at 0.65 V vs. Ag/AgCl. This is in part due to enhanced surface to volume ratio on the electrode surface and facilitation of electron transfer, but selectivity and surface reusability is also an important concern for a multiplexed device. The observed decrease in current associated with the follow-on oxidation species provides reason to believe that this modified surface can assist where multiple components are of interest e.g. in presence of 1,3-diethyl-1,3-diphenylurea (ethyl Centralite) as a co-target in forensic analysis. A postulated mechanism for this signal enhancement is given below with DPA generating Fe^{2+} from Fe^{3+} species (dominant at pH 4.5) [41].

$$DPA_{(red)} + [Fe(OH)]^{2+} \rightarrow DPA_{(ox)} + Fe^{2+} + H_2O$$

In order to examine lower analytical ranges Fig. 11 shows differential pulse voltammograms over the range −1 to 1.5 V (A) with focus on relevant potential range of DPA oxidation (B) and corresponding calibration curve for the MNP modified electrodes (C) over the range concentration range 0.5–50 μM n = 3 (SD = 1.27×10^{-6} A cm^{-2}) with sensitivity 1.13×10^{-3} A cm^{-2} mM^{-1}, LOD = 3.51×10^{-6} M, LOQ = 1.17×10^{-5} M relative to unmodified electrode with LOD = 2.27×10^{-6} M, LOQ = 7.57×10^{-6} M and sensitivity 9.80×10^{-4} A cm^{-2} mM^{-1}.

3.6. Real sample analysis

Firearm residue samples were processing according to the method described in section 2.2.6 with data shown in Fig. 12. Unburnt propellant was extracted and underwent DPV analysis (Fig. 12(A)) and qualitative identification of the DPA signal at E_p = 0.676 V vs. Ag/AgCl was confirmed by overlaying with a 10 μM DPA standard DPV, in the case of both bare and MNP modified electrodes. A wave representing lead oxidation appeared at −0.492 V, which matches previous reports under similar experimental conditions [53], and the signal was observed to be significantly amplified at the MNP modified electrode with an average

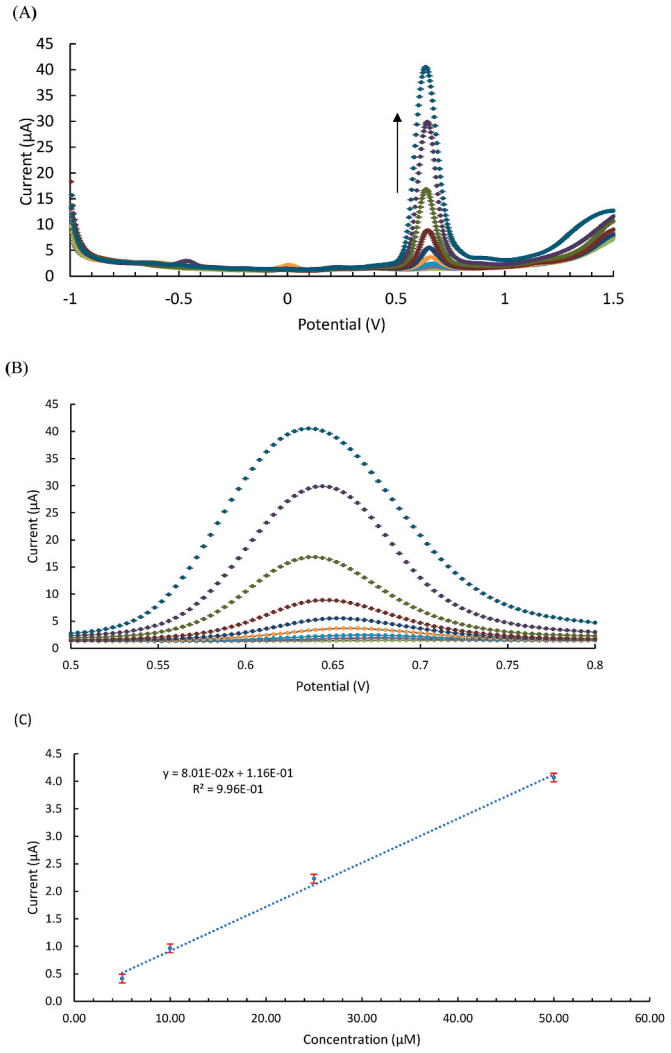

Fig. 11. (A) Differential pulse voltammograms (average current with error bars) for MNP modified GCE over the range −1 to 1.5 V vs. Ag/AgCl, in increments of 0.004 V at an amplitude of 0.05 V with a pulse width of 0.05 s and a pulse period of 0.5 s, in methanol/sodium acetate buffer (3:7) over the range 0.5–1000 μM with zoomed in region (B) between 0.5 and 0.8 V and corresponding calibration curve (C) showing linearity over the range 0.5–50 μM for the MNP modified surface (n = 3).

37 fold increase in current observed. This is thought to be due to the co-ordination of Pb^{2+} ions to the surface hydroxy groups of the magnetic nanomaterials, with the lead response being sensitive to nanomaterial loading/dispersion with intra electrode variations. Xiong et al., 2013 demonstrated a similar effect at amine functionalised magnetite nanoparticles with a 10 fold enhancement in signal using a stripping square wave approach [54]. Wu et al. also reported a mixed metal quantitative system made possible at Fe_3O_4 modified functionalised multiwalled carbon nanotubes [55].

To our knowledge no such report of simultaneous metal and organic firearm residue has been reported using a magnetic nanoparticle modified electrode. Fig. 12 (A) shows the unburnt propellant DPV overlaid with standard voltammograms at both bare and modified electrodes. Standard addition followed (Fig. 12 (B)) with additions of DPA over the range 19.6–56.6 mM realising 10.7 ± 0.3 mg/g of DPA in the unburnt propellant. Fig. 12 (C) shows the firearm residue DPV trace following recovery via methanol swabbing of the textile surface. MNP modified electrodes resulted in a wave at 0.672 V indicative of DPA which was confirmed by spiking (19.6–56.6 mM DPA additions). Quantitation realised 25.2 μM ± 5.5 μM representing a recovery of

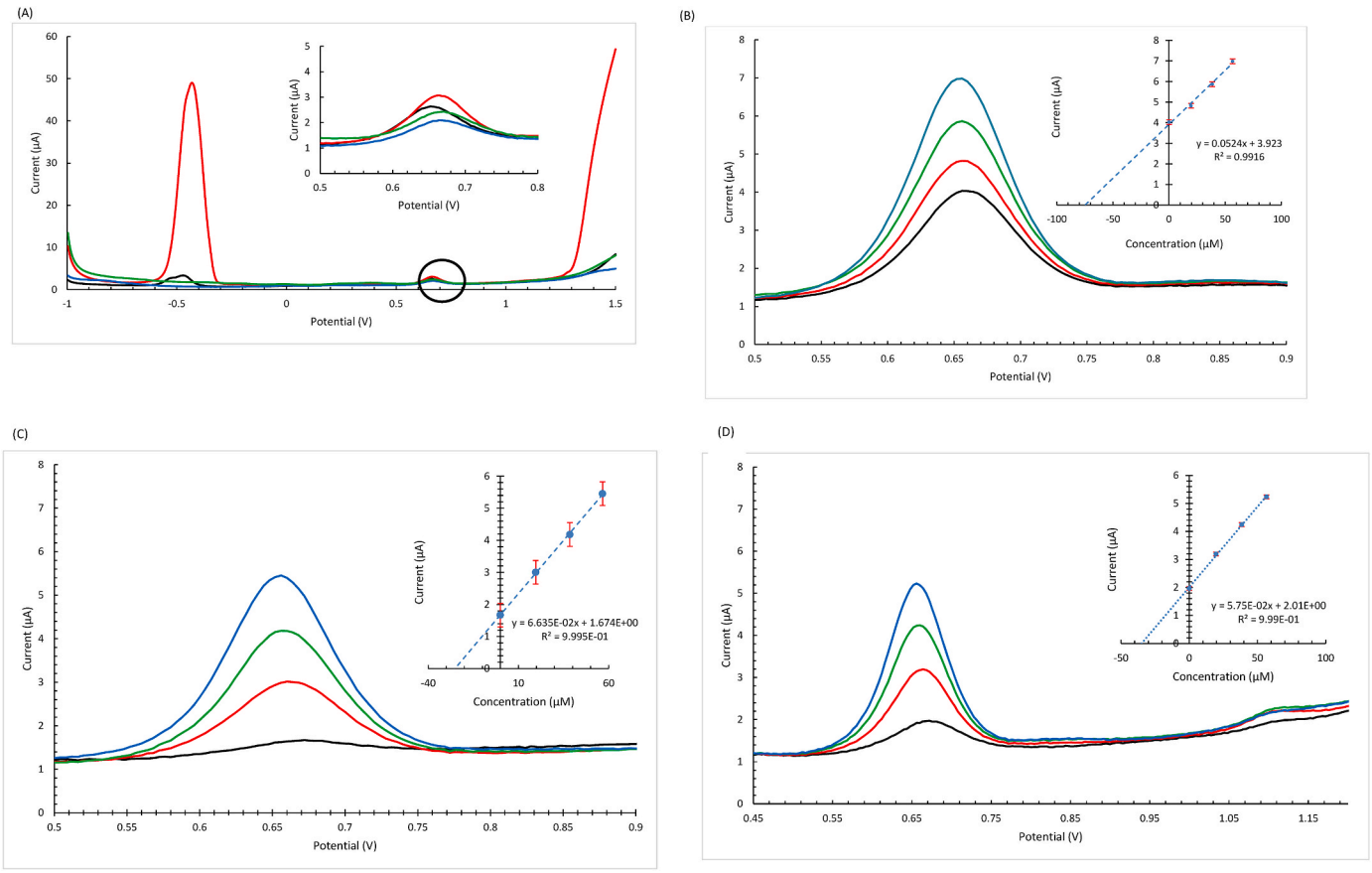

Fig. 12. (A) Comparison (n = 3) of unburnt propellent at bare (Black) and MNP modified (Red) electrodes and 10 μM DPA standard at bare (Blue) and MNP modified (Green) electrodes; DPVs (average n = 3) at MNP modified GCE with standard addition of DPA 19.6–56.6 μM (B) recovered unburned propellent (C) gunshot residue sample recovered via swabbing (D) recovered gunshot residue from spent cartridge: recovered sample (Black), addition of 19.6 μM (Red), 38.5 μM (Green) 56.6 μM (Blue) DPA. (For interpretation of the references to colour in this figure legend, the reader is referred to the Web version of this article.)

0.427 μg/cm^2 (21.3 μg in total) of OGSR swab area. Finally, Fig. 12 (D) represents electroanalysis of the fired cartridge (internal area ~37.7 cm^2) with DPA standard addition over the same range resulting in recovery of 0.783 μg/cm^2 (29.5 μg in total). The wave at E_p = 1.112 V is indicative of Centralite stabiliser residue, to be examined more thoroughly in the next phase of the work.

Table 3 summarises chromatography and spectroscopic approaches to identification of OGSR in forensic chemical analysis with many focusing on qualitative identification of residues. GC-MS is used widely, however, artefacts can be formed during analysis and degradation can occur once compounds are exposed to the heat of injection, therefore complementary analysis via lower cost non-laboratory confined approaches have significant merit. In relation to quantitative electroanalytical approaches at modified electrodes, comparative analytical performance data for forensic electroanalysis of DPA at modified electrodes is constrained by few reports in the literature with the sole exception of Sakthievel et al. (2018) reporting a EuMoSe modified GCE resulting in LOD of 8.8 nA [17] for DPA quantitation in apple juice. Other reports in relation to gunshot residue [11,56] realised DPA quantitation at bare GCE and screen printed electrodes resulting in detection in the μM range. The chemically modified electrode proposed here has demonstrated comparable analytical performance and is unique in so far as it has its basis in an examination of DPA redox behaviour at electrosynthesised magnetic nanoparticle modified GCEs. The reproducibility of the MNP application to the GCE was examined in the case of the DPV study and it was observed that the drop casting method led to slightly wider variation (SD = 9.36 × 10^{-8} A (n = 9)) when compared to its bare counterpart (SD = 5.24 × 10^{-8} A (n = 9)).

4. Conclusions

The work was motivated by the on-going demand for organic residue rapid testing as a tool for onsite use by forensic scientists and the lack of reports of modified electrodes for propellant stabiliser residue analysis. Being able to measure molecules that survive the firing event opens new opportunities for trace analysis and persistence studies. Persistence times of OGSR on the hands of the shooter are typically 4 h with half-life of 1 h so time is of the essence in relation to detection [58] and the methodology proposed here is capable of sample to result within <2 min.

We have also advanced understanding of the electrooxidation of DPA in organic and aqueous electrolytes realising key insights into follow up products and processes which could arise during degradation. The work presented progresses this via a successful study into the electrochemistry of DPA coupled with the first time use of iron oxide magnetic nanoparticles, positively influencing the sensing capabilities of the modified GCE.

MNPs were prepared using the accessible and controlled process of electrooxidation at iron anodes followed by characterisation via surface, thermal, spectroscopic and electrochemical techniques. DPA redox activity was probed in both aqueous and non – aqueous environments (D values 1.43 × 10^{-6} and 5.47 × 10^{-8} cm^2 s^{-1} respectively). The cathodic limit influenced the redox process of the surface confined MNP and also enhanced the DPA electrooxidation which was followed by formation of a surface confined electroactive product of the initial oxidation step. Peaks associated with the latter process diminished at the MNP electrode which has benefits of signal reproducibility upon cycling and calibration. Spectroelectrochemical studies pointed to the formation of poly

Table 3
Summary of analytical approaches to DPA analysis.

Method	Linear range	LOD (Absolute detection limit)\2	LOD (μg/mL)	Reference
[a]Solid phase microextraction GC (qualitative)	–	–	–	[57]
[a]Ion mobilise spectrometry			–	[58]
[a]Transfer to TLC with luminescence detection(qualitative)	–	–	–	[52]
[a]GC-MS	–	–	–	[59]
[a]UHPLC-ESI-MS/MS	–	–	–	[60]
[a]Surface enhanced Raman spectroscopy	–	–	–	[61]
MS/MS	–	–	1 ng/mL	[62]
Solid phase microextraction with ion mobility spectrometer	–	0.12–1.2 ng		[63]
Thermal desorption GC-MS		5 ng	–	[64]
LC-EC detector (Au/Hg)	–	0.039 ng	–	[65]
HPLC tandem MS/MS	0.029–2.95 μM	–	3×10^{-4}	[66]
$EuMoSe_2$/GCE	–	8.8 nM	1.49×10^{-3}	[17]
Glassy carbon disk	Up to 188 μM	–	–	[11]
C-SPE	9.4–188 μM	–	0.4	[56]
Bare GCE	*0.5* - 50 μM	*0.*384 μg/mL	*0.384*	*This work*
MNP modified GCE	*0.5* - 50 μM	*0.*594 μg/mL[a]	*0.594*	*This Work*

[a] These articles reported qualitative forensic detection of DPA in addition to other organic components of gunshot residue.

(diphenylamine) via potential cycling on a Pt gauze electrode (λ max = 456 nm).

DPA quantitation was achieved via differential pulse voltammetry realising precise (SD = 9.36×10^{-8} A for n = 9) and robust analytical performance with sensitivity 1.13×10^{-3} A cm^{-2} mM^{-1}. Real sample analysis of both unburnt and firearm propellant residue realised qualitative and quantitative DPA analysis resulting in clear signals for the stabiliser residue in addition to the main metal residue (lead), both of which were found to be enhanced by the magnetic nanoparticles. Recovery and DPA spiking studies were performed in the base of an unburnt propellant powder sample and the recovered residue, realising 10.7 ± 0.3 mg/g and 0.427 μg/cm^2 (21.3 μg in total) respectively.

Further work in our group will progress a total analysis system for firearm residue with development of ferrofluids (graphite inks with inclusion of MNP) with capability for thick film transducer printing with extension to ethyl centralite following residue sample recovery via tape lift/integrated solvent swob including persistence studies. This will include testing of OGSR swobs with integrated sample collection - screen printed electrode transducer.

Overall, this work makes a positive contribution to (a) the currently limited number of reports of electrochemical synthesis and optimisation of magnetic nanoparticles with optimisation and full characterisation (b) the novel examination of the influence of this modifier on quantitation of DPA propellant stabiliser using both CV and DPV (c) our means to realise a rapid analytical test for forensic chemical analysis of the organic components of firearm residue.

Declaration of competing interest

The authors declare that they have no known competing financial interests or personal relationships that could have appeared to influence the work reported in this paper.

Acknowledgements

The authors would like to acknowledge the Dept. Chemistry PhD Teaching Fellowship, Maynooth University and University of Limerick for XRD analysis.

Appendix A. Supplementary data

Supplementary data to this article can be found online at https://doi.org/10.1016/j.talanta.2021.123039.

Credit author statement

Colm McKeever: Methodology, Formal analysis, Investigation; Data curation, Writing – review & editing. **Sarah Callan:** Data curation, Methodology, Investigation. **Susan Warren:** Data curation, Formal analysis. **Eithne Dempsey:** Conceptualisation, Investigation, Formal analysis, Funding acquisition, Project administration, Writing – review & editing.

References

[1] A.M. O'Mahony, J. Wang, Electrochemical detection of gunshot residue for forensic analysis: a review, Electroanalysis 25 (2013) 1341–1358.
[2] J.C.D. Freitas, J.E.S. Sarkis, O.N. Neto, S.B. Viebig, Identification of gunshot residues in fabric targets using sector field inductively coupled plasma mass spectrometry technique and ternary graphs, J. Forensic Sci. 57 (2012) 503–508, https://doi.org/10.1111/j.1556-4029.2011.01956.x.
[3] C.R. Vachon, M.V. Martinez, Understanding gunshot residue evidence and its role in forensic science, Am. J. Forensic Med. Pathol 40 (2019) 210–219.
[4] L. Shaw, L. Dennany, Applications of electrochemical sensors: forensic drug analysis, Curr. Opin. Electrochem. 3 (2017) 23–28, https://doi.org/10.1016/j.coelec.2017.05.001.
[5] P. Pigou, G.H. Dennison, M. Johnston, H. Kobus, An investigation into artefacts formed during gas chromatography/mass spectrometry analysis of firearms propellant that contains diphenylamine as the stabiliser, Forensic Sci. Int. 279 (2017) 140–147, https://doi.org/10.1016/j.forsciint.2017.08.013.
[6] H.A. Yu, D.A. DeTata, S.W. Lewis, D.S. Silvester, Recent developments in the electrochemical detection of explosives: towards field-deployable devices for forensic science, TrAC Trends Anal. Chem. (Reference Ed.) 97 (2017) 374–384, https://doi.org/10.1016/j.trac.2017.10.007.
[7] O. Dalby, D. Butler, J.W. Birkett, Analysis of gunshot residue and associated materials - a review, J. Forensic Sci. 55 (2010) 924–943, https://doi.org/10.1111/j.1556-4029.2010.01370.x.
[8] A.I. Argente-García, L. Hakobyan, C. Guillem, P. Campíns-Falcó, Estimating diphenylamine in gunshot residues from a new tool for identifying both inorganic and organic residues in the same sample, Separations 6 (2019), https://doi.org/10.3390/separations6010016.
[9] A. Bergens, K. Lundstrbm~, J. Asplund, VOLTAMMETRIC DETERMINATION OF THE STABILIZING ADDITIVES ACARDITE II, CENTRALITE I AND DIPHENYLAMINE IN PROPELLANTS, 1985.
[10] E. Parliament, E. Parliament, E. Parliament, COMMISSION REGULATION (EU) 2018/1515 of 10 October 2018, 2018, 2018.
[11] M. Vuki, K.K. Shiu, M. Galik, et al., Simultaneous electrochemical measurement of metal and organic propellant constituents of gunshot residues, Analyst 137 (2012) 3265–3270, https://doi.org/10.1039/c2an35379b.
[12] H. Yang, A.J. Bard, The application of rapid scan cyclic voltammetry and digital simulation to the study of the mechanism of diphenylamine oxidation, radical cation dimerization, and polymerization in acetonitrile, J. Electroanal. Chem. 306 (1991) 87–109, https://doi.org/10.1016/0022-0728(91)85224-D.
[13] R.V. Taudte, C. Roux, A. Beavis, Stability of smokeless powder compounds on collection devices, Forensic Sci. Int. 270 (2017) 55–60, https://doi.org/10.1016/j.forsciint.2016.11.027.
[14] U. Hayat, P.N. Bartlett, G.H. Dodd, J. Barker, Electrochemical synthesis and study of polydiphenylamine, J. Electroanal. Chem. 220 (1987) 287–294, https://doi.org/10.1016/0022-0728(87)85115-X.
[15] A.V. Orlov, S.Z. Ozkan, G.P. Karpacheva, Oxidative polymerization of diphenylamine: a mechanistic study, Polym. Sci. B 48 (2006) 11–17, https://doi.org/10.1134/S1560090406010039.
[16] G. Inzelt, Cyclic voltammetry of solid diphenylamine crystals immobilized on an electrode surface and in the presence of an aqueous solution, J. Solid State Electrochem. 6 (2002) 265–271, https://doi.org/10.1007/s100080100223.
[17] M. Sakthivel, R. Sukanya, S.M. Chen, Fabrication of europium doped molybdenum diselenide nanoflower based electrochemical sensor for sensitive detection of diphenylamine in apple juice, Sensor. Actuator. B Chem. 273 (2018) 616–626, https://doi.org/10.1016/j.snb.2018.06.094.
[18] H.N. Abdelhamid, Nanoparticle-based surface assisted laser desorption ionization mass spectrometry: a review, Microchim Acta 186 (2019), https://doi.org/10.1007/s00604-019-3770-5.

[19] G.K. Kouassi, J. Irudayaraj, G. McCarty, Examination of cholesterol oxidase attachment to magnetic nanoparticles, J. Nanobiotechnol. 3 (2005) 1–9, https://doi.org/10.1186/1477-3155-3-1.

[20] P. Theamdee, R. Traiphol, B. Rutnakornpituk, et al., Surface modification of magnetite nanoparticle with azobenzene-containing water dispersible polymer, J. Nanoparticle Res. 13 (2011) 4463–4477, https://doi.org/10.1007/s11051-011-0399-7.

[21] S.F. Wang, F. Xie, R.F. Hu, Carbon-coated nickel magnetic nanoparticles modified electrodes as a sensor for determination of acetaminophen, Sensor. Actuator. B Chem. 123 (2007) 495–500, https://doi.org/10.1016/j.snb.2006.09.031.

[22] J. Wallyn, N. Anton, T.F. Vandamme, Synthesis, principles, and properties of magnetite nanoparticles for in vivo imaging applications—a review, Pharmaceutics 11 (2019) 1–29, https://doi.org/10.3390/pharmaceutics11110601.

[23] Y. Chang, Y. Bai, B. Teng, Z. Li, A new drug carrier: magnetite nanoparticles coated with amphiphilic block copolymer, Chin. Sci. Bull. 54 (2009) 1190–1196, https://doi.org/10.1007/s11434-009-0144-0.

[24] R. Doaga, T. McCormac, E. Dempsey, Functionalized magnetic nanomaterials for electrochemical biosensing of cholesterol and cholesteryl palmitate, Microchim Acta 187 (2020), https://doi.org/10.1007/s00604-020-4203-1.

[25] B.W. Lu, W.C. Chen, A disposable glucose biosensor based on drop-coating of screen-printed carbon electrodes with magnetic nanoparticles, J. Magn. Magn Mater. 304 (2006) 400–402, https://doi.org/10.1016/j.jmmm.2006.01.222.

[26] D. Martín-Yerga, Electrochemical detection and characterization of nanoparticles with printed devices, Biosensors 9 (2019), https://doi.org/10.3390/bios9020047.

[27] M. Hasanzadeh, N. Shadjou, M. de la Guardia, Iron and iron-oxide magnetic nanoparticles as signal-amplification elements in electrochemical biosensing, TrAC Trends Anal. Chem. (Reference Ed.) 72 (2015) 1–9, https://doi.org/10.1016/j.trac.2015.03.016.

[28] G. Priyadarshana, N. Kottegoda, A. Senaratne, et al., Synthesis of magnetite nanoparticles by top-down approach from a high purity ore, J. Nanomater. (2015), https://doi.org/10.1155/2015/317312, 2015.

[29] Z.E. Gahrouei, S. Labbaf, A. Kermanpur, Cobalt doped magnetite nanoparticles: synthesis, characterization, optimization and suitability evaluations for magnetic hyperthermia applications, Phys. E Low Dimens. Syst. Nanostruc. 116 (2020) 113759, https://doi.org/10.1016/j.physe.2019.113759.

[30] L. Del Bianco, F. Spizzo, G. Barucca, et al., Mechanism of magnetic heating in Mn-doped magnetite nanoparticles and the role of intertwined structural and magnetic properties, Nanoscale 11 (2019) 10896–10910, https://doi.org/10.1039/c9nr03131f.

[31] D. Ramimoghadam, S. Bagheri, S.B.A. Hamid, Progress in electrochemical synthesis of magnetic iron oxide nanoparticles, J. Magn. Magn Mater. 368 (2014) 207–229, https://doi.org/10.1016/j.jmmm.2014.05.015.

[32] B. Sun, X. Ni, Y. Cao, G. Cao, Electrochemical sensor based on magnetic molecularly imprinted nanoparticles modified magnetic electrode for determination of Hb, Biosens. Bioelectron. 91 (2017) 354–358, https://doi.org/10.1016/j.bios.2016.12.056.

[33] L. Cabrera, S. Gutierrez, N. Menendez, et al., Magnetite nanoparticles: electrochemical synthesis and characterization, Electrochim. Acta 53 (2008) 3436–3441, https://doi.org/10.1016/j.electacta.2007.12.006.

[34] N. Rahimdad, A. Khalaj, G. Azarian, D. Nematollahi, Electrochemical device for the synthesis of Fe 3 O 4 magnetic nanoparticles, J. Electrochem. Soc. 166 (2019) E1, https://doi.org/10.1149/2.0231902jes. –E6.

[35] MAXAM Powders. Powders. Accessed 29 Jun 2021 www.maxamcorp.com/en/cartridges-components/components/powder.

[36] N. Habibi, Preparation of biocompatible magnetite-carboxymethyl cellulose nanocomposite: characterization of nanocomposite by FTIR, XRD, FESEM and TEM, Spectrochim. Acta Part A Mol Biomol Spectrosc 131 (2014) 55–58, https://doi.org/10.1016/j.saa.2014.04.039.

[37] J.P. Wright, A.M.T. Bell, J.P. Attfield, Variable temperature powder neutron diffraction study of the Verwey transition in magnetite Fe3O4, Solid State Sci. 2 (2000) 747–753, https://doi.org/10.1016/S1293-2558(00)01107-9.

[38] M. Starowicz, P. Starowicz, J. Żukrowski, et al., Electrochemical synthesis of magnetic iron oxide nanoparticles with controlled size, J. Nanoparticle Res. 13 (2011) 7167–7176, https://doi.org/10.1007/s11051-011-0631-5.

[39] M.E. Fleet, The Structure of Magnetite: Symmetry of Cubic Spinels, 1986.

[40] M. Ristić, T. Fujii, H. Hashimoto, et al., A novel route in the synthesis of magnetite nanoparticles, Mater. Lett. 100 (2013) 93–97, https://doi.org/10.1016/j.matlet.2013.03.013.

[41] K. Yuan, D. Renock, R.C. Ewing, U. Becker, Uranium reduction on magnetite: probing for pentavalent uranium using electrochemical methods, Geochem. Cosmochim. Acta 156 (2015) 194–206, https://doi.org/10.1016/j.gca.2015.02.014.

[42] Y.J. Kim, K. Yuan, B.R. Ellis, U. Becker, Redox reactions of selenium as catalyzed by magnetite: lessons learned from using electrochemistry and spectroscopic methods, Geochem. Cosmochim. Acta 199 (2017) 304–323, https://doi.org/10.1016/j.gca.2016.10.039.

[43] E.P. Achterberg, Laboratory Techniques in Electroanalytical Chemistry, second ed., Marcel Dekker, INC, 1996.

[44] T.H. Tsai, S.H. Ku, S.M. Chen, et al., Electropolymerized diphenylamine on functionalized multiwalled carbon nanotube composite film and its application to develop a multifunctional biosensor, Electroanalysis 26 (2014) 399–408, https://doi.org/10.1002/elan.201300495.

[45] R.G. Krishnan, B. Saraswathyamma, Simultaneous resolution and electrochemical quantification of tyrosine and tryptophan at a poly (diphenylamine) modified electrode, J. Electrochem. Soc. 168 (2021), 027509, https://doi.org/10.1149/1945-7111/abe1dd.

[46] S. Golczak, A. Kanciurzewska, M. Fahlman, et al., Comparative XPS surface study of polyaniline thin films, Solid State Ionics 179 (2008) 2234–2239, https://doi.org/10.1016/j.ssi.2008.08.004.

[47] E. Food, S. Authority, Conclusion on the peer review of the pesticide risk assessment of the active substance diphenylamine, EFSA J. 10 (2012) 1–59, https://doi.org/10.2903/j.efsa.2012.2486.

[48] S. Nagarajan, P. Santhosh, M. Sankarasubramanian, et al., UV-vis spectroscopy for following the kinetics of homogeneous polymerization of diphenylamine in p-toluene sulphonic acid, Spectrochim. Acta Part A Mol Biomol Spectrosc 62 (2005) 420–430, https://doi.org/10.1016/j.saa.2005.01.010.

[49] Y.T. Tsai, T.C. Wen, A. Gopalan, Tuning the optical sensing of pH by poly (diphenylamine), Sensor. Actuator. B Chem. 96 (2003) 646–657, https://doi.org/10.1016/j.snb.2003.07.009.

[50] M.S. Wu, T.C. Wen, A. Gopalan, In situ UV-visible spectroelectrochemical studies on the copolymerization of diphenylamine with anthranilic acid, Mater. Chem. Phys. 74 (2002) 58–65, https://doi.org/10.1016/S0254-0584(01)00406-0.

[51] Naqvi II, A. Perveen, Investigation of electron transfer reaction between diphenylbenzidine and ascorbic acid, Turk. J. Chem. 29 (2005) 627–634.

[52] R. Hofer, P. Wyss, The use of unburned propellant powder for shooting-distance determination. Part II: diphenylamine reaction, Forensic Sci. Int. 278 (2017) 24–31, https://doi.org/10.1016/j.forsciint.2017.06.022.

[53] R. Segura, K. DÍAz, J. Pizarro, et al., Anodic stripping voltammetric determination of lead using a chemically modified electrode based on AZA crown ether, J. Chil. Chem. Soc. 62 (2017) 3726–3730, https://doi.org/10.4067/s0717-97072017000403726.

[54] S. Xiong, M. Wang, D. Cai, et al., Electrochemical detection of Pb(II) by glassy carbon electrode modified with amine-functionalized magnetite nanoparticles, Anal. Lett. 46 (2013) 912–922, https://doi.org/10.1080/00032719.2012.747094.

[55] W. Wu, M. Jia, Z. Wang, et al., Simultaneous voltammetric determination of cadmium(II), lead(II), mercury(II), zinc(II), and copper(II) using a glassy carbon electrode modified with magnetite (Fe3O4) nanoparticles and fluorinated multiwalled carbon nanotubes, Microchim Acta 186 (2019), https://doi.org/10.1007/s00604-018-3216-5.

[56] C.E. Ott, K.A. Dalzell, P.J. Calderón-Arce, et al., Evaluation of the simultaneous analysis of organic and inorganic gunshot residues within a large population data set using electrochemical sensors, J. Forensic Sci. 1–10 (2020), https://doi.org/10.1111/1556-4029.14548.

[57] G.L. Burleson, B. Gonzalez, K. Simons, J.C.C. Yu, Forensic analysis of a single particle of partially burnt gunpowder by solid phase micro-extraction-gas chromatography-nitrogen phosphorus detector, J. Chromatogr. A 1216 (2009) 4679–4683, https://doi.org/10.1016/j.chroma.2009.03.074.

[58] J. Arndt, S. Bell, L. Crookshanks, et al., Preliminary evaluation of the persistence of organic gunshot residue, Forensic Sci. Int. 222 (2012) 137–145, https://doi.org/10.1016/j.forsciint.2012.05.011.

[59] M. Maitre, M. Horder, K.P. Kirkbride, et al., A forensic investigation on the persistence of organic gunshot residues, Forensic Sci. Int. 292 (2018) 1–10, https://doi.org/10.1016/j.forsciint.2018.08.036.

[60] C. Bonnar, E.C. Moule, N. Lucas, et al., Tandem detection of organic and inorganic gunshot residues using LC–MS and SEM-EDS, Forensic Sci. Int. 314 (2020) 110389, https://doi.org/10.1016/j.forsciint.2020.110389.

[61] M. López-López, V. Merk, C. García-Ruiz, J. Kneipp, Surface-enhanced Raman spectroscopy for the analysis of smokeless gunpowders and macroscopic gunshot residues, Anal. Bioanal. Chem. 408 (2016) 4965–4973, https://doi.org/10.1007/s00216-016-9591-z.

[62] Y. Tong, Z. Wu, C. Yang, et al., Determination of diphenylamine stabilizer and its nitrated derivatives in smokeless gunpowder using a tandem MS method, Analyst 126 (2001) 480–484, https://doi.org/10.1039/b010183o.

[63] M. Joshi, Y. Delgado, P. Guerra, et al., Detection of odor signatures of smokeless powders using solid phase microextraction coupled to an ion mobility spectrometer, Forensic Sci. Int. 188 (2009) 112–118, https://doi.org/10.1016/j.forsciint.2009.03.032.

[64] B. Stevens, S. Bell, K. Adams, Initial evaluation of inlet thermal desorption GC–MS analysis for organic gunshot residue collected from the hands of known shooters, Forensic Chem. 2 (2016) 55–62, https://doi.org/10.1016/j.forc.2016.10.001.

[65] K. Bratin, P.T. Kissinger, R.C. Briner, C.S. Bruntlett, Determination of nitro aromatic, nitramine, and nitrate ester explosive compounds in explosive mixtures and gunshot residue by liquid chromatography and reductive electrochemical detection, Anal. Chim. Acta 130 (1981) 295–311, https://doi.org/10.1016/S0003-2670(01)93007-7.

[66] H. Mei, Y. Quan, W. Wang, et al., Determination of diphenylamine in gunshot residue by HPLC-MS/MS, J. Forensic Sci. Med. 2 (2016) 18–21, https://doi.org/10.4103/2349-5014.162808.